RESEARCH ARTICLE

Check for updates

Bifunctional electroreduction catalysts of NiFe alloy on N-doped carbon toward industrial-level CO₂ conversion powered by Zn–air batteries†

Songjiang Wu,‡[a] Haiyan Chen,‡[a] Chunguang Jia,[a] Li Liao,[a] Kai Chen,[b] Suqin Ci,*[a] Qiuhua Xu[a] and Zhenhai Wen 🔘 *[a,b]

We present a facile pyrolysis method for the synthesis of nitrogen-doped carbon-supported NiFe alloys (NiFe-NC) that exhibit excellent electrocatalytic activity for both the CO₂ reduction reaction (CO₂RR) and the oxygen reduction reaction (ORR). Notably, the NiFe-NC catalyst demonstrates an unprecedented CO₂RR activity with a CO faradaic efficiency (FE) of 93.42% at −0.58 V *vs.* RHE. In addition, NiFe-NC in a flow cell reactor achieves an industrial current density of 241.09 mA cm⁻² with a high CO FE of 91.6%. Furthermore, the NiFe-NC catalyst shows an impressive ORR performance, with an onset potential of 0.967 V *vs.* RHE and a half-wave potential of 0.867 V *vs.* RHE, which is comparable to that of commercial Pt/C catalysts. We demonstrate the potential of NiFe-NC as a cathode material in Zn–air batteries (ZABs), achieving a maximum power density of 185.92 mW cm⁻². Importantly, a self-driven CO₂ flow electrolysis system powered by two series-connected NiFe-NC-based ZABs is designed. This innovative system demonstrates high efficiency in converting CO₂ to CO, with a continuous operation time of up to 27 h. According to theoretical calculations, the NiFe-NC catalyst contains Ni-ApyNH and Fe-GN sites, which exhibit remarkable activity in ORR and CO₂RR, respectively. The superior bifunctional electrocatalytic performance of NiFe-NC makes it a promising candidate for a wide range of applications. We anticipate that the results of our approach and the exploration of the exact active site of the catalyst will stimulate further studies on the development of efficient electrocatalysts for energy conversion and storage.

1. Introduction

The urgent need to address the challenges of rapid fossil fuel consumption and global warming has led to a surge in research on sustainable energy.[1,2] Electrochemical CO₂ reduction for fuel generation and the development of metal–air batteries are among the promising strategies,[3–5] involving the CO₂ reduction reaction (CO₂RR) and the oxygen reduction reaction (ORR). These reactions are kinetically slow and require efficient catalysts to enhance their activity.[6–9] While precious metals such as Au and Ag have shown good electrocatalytic properties, their high cost, low stability, and limited applicability to single reactions impede their commercial application.[10,11] Therefore, the exploration of non-noble metal electrocatalysts with fast kinetics, high activity, and good durability is essential. Transition metal-based catalysts such as Ni-, Fe-, and Co-based catalysts have been extensively investigated for their cost-effectiveness and good catalytic activity.[12–15] However, their practical use is limited by their poor stability and low conversion efficiency. Among the various catalysts that have been studied, alloy catalysts have emerged as a promising option due to their ability to reduce the kinetic overpotential and control selectivity.[16,17] Additionally, the low solubility of CO₂ in the electrolyte and limited mass transfer of CO₂ in the H-cell hinder the CO₂ reduction kinetics, making it difficult to achieve industrial-grade current levels of >200 mA cm⁻².[18] In contrast, gas diffusion electrodes (GDEs) in a flow cell can significantly improve the gas transport efficiency by efficiently transporting CO₂ from the gas phase to the catalyst surface, resulting in a 2-order-of-magnitude improvement in CO₂RR reactivity compared to the H-cell. Therefore, the study of flow cells is necessary to achieve industrial current densities.[19–23]

Iron-based catalysts have been reported to exhibit low CO₂RR onset potentials. However, the strong binding of iron sites to reaction intermediates, such as *CO, severely reduces

ªKey Laboratory of Jiangxi Province for Persistent Pollutants Control, National–Local Joint Engineering Research Center of Heavy Metals Pollutants Control and Resource Utilization and Resources Recycle, Nanchang Hangkong University, Nanchang 330063, Jiangxi, China. E-mail: sqci@nchu.edu.cn, wen@fjirsm.ac.cn
ᵇCAS Key Laboratory of Design and Assembly of Functional Nanostructures, and Fujian Provincial Key Laboratory of Materials and Techniques toward Hydrogen Energy, Fujian Institute of Research on the Structure of Matter, Chinese Academy of Sciences, Fuzhou, Fujian, 350002, China
†Electronic supplementary information (ESI) available. See DOI: https://doi.org/10.1039/d3qi00966a
‡These authors contributed equally to this work.

4484 | *Inorg. Chem. Front.*, 2023, **10**, 4484–4495

This journal is © the Partner Organisations 2023

the faradaic efficiency, as evidenced in previous studies.[24,25] In contrast, nickel-based catalysts display high current densities and faradaic efficiencies in CO_2RR, but their larger onset potentials are attributed to the high energy potential required for the formation of *COOH intermediates.[26,27] Compared to monometallic-based catalysts, alloyed catalysts composed of two metals may achieve complementary functions and synergistic effects that can tune the optimized binding energy to intermediates and enhance the intrinsic catalytic activity and selectivity.[28,29] Nevertheless, the development of easily and rationally constructed alloy catalysts with high catalytic performance and multifunctionality, and the elucidation of their primary active sites, remain significant challenges.

Herein, we report the facile synthesis of an efficient bifunctional material (NiFe-NC), derived from a metal–organic framework precursor. The outstanding CO selectivity of 93.42% at 0.58 V *vs.* RHE during CO_2RR is achieved by the unique bimetallic sites present in the NiFe-NC catalyst. Impressively, the NiFe-NC catalyst exhibits remarkable stability by retaining an exceptional CO faradaic efficiency of 91.6% even under high current density conditions of 241.09 mA cm^{-2} in the flow cell reactor, surpassing the value in the H-cell by more than an order of magnitude. Furthermore, we have demonstrated the capability of NiFe-NC as a cathode material in Zn–air batteries (ZABs), achieving a remarkable power density of 185.92 mW cm^{-2}. We also design a self-driven CO_2 flow electrolysis system that is powered by two homemade ZABs connected in series, and this system has shown excellent efficiency in converting CO_2 to CO. Additionally, theoretical calculations are used to explore the possible active sites of NiFe-NC, and the results indicate that the Ni-ApyNH site and the Fe-GN site are the best catalytic active sites for ORR and CO_2RR, respectively. The coexistence of the two sites results in excellent bifunctional catalytic activity of NiFe-NC. These results highlight the tremendous potential of NiFe-NC as a versatile and highly efficient catalyst for sustainable energy storage and conversion applications.

2. Results and discussion

2.1. Catalyst characterization

The synthetic route of NiFe-NC is presented in Fig. 1a. Initially, NiFe-ZIF-8 precursors were obtained by mixing nickel acetate, iron nitrate, zinc nitrate, and 2-methylimidazole. Subsequently, NiFe-NC was synthesized by pyrolyzing the precursors at 1000 °C under an argon atmosphere. We also synthesized a series of catalysts by the same route for comparison, including NiFe-NC, Ni-NC, Fe-NC, NC, NiFe-NC-900, and NiFe-NC-1100. The SEM images reveal that the morphology of NiFe-NC is a uniform rhombic dodecahedron with an average diameter of ~100 nm (Fig. S1a–f†).[30] The TEM images of NiFe-NC (Fig. 1b–d) further confirm the structure of the rhombic dodecahedron, where NiFe nanoparticles are encapsulated in a nitrogen-doped carbon shell. The high-resolution TEM (HRTEM) image exhibits a lattice fringe of 0.209 nm (Fig. 1e

and f), corresponding well with the (111) lattice plane of the NiFe alloy. Meanwhile, the crystal plane spacing of the carbon layer coated with nanoparticles is 0.34 nm, which belongs to the (002) crystal plane of graphitic carbon. The carbon layer present on the surface of the NiFe alloy nanoparticles ensures that reactants have access to the NiFe core while also preventing the NiFe alloy nanoparticles from oxidizing due to air exposure or aggregation. These characteristics are essential for maintaining high electrocatalytic activity and long-term stability.[31] Additionally, the high-angle annular dark field scanning transmission electron microscopy (HAADF-STEM) and EDS element mapping images of NiFe-NC (Fig. 1g) confirm the coexistence and dispersion of Fe, Ni, and N atoms. Fe and Ni are concentrated in the nanoparticles, indicating the formation of the NiFe alloy.

The X-ray powder diffraction (XRD) pattern of NiFe-NC is depicted in Fig. 2a. The peaks at 43.49°, 50.67°, and 74.54° can be assigned to the (111), (200), and (220) planes of the taenite, *syn* (Fe, Ni) phase (JPCDS no. 47-1417).[32] The peaks in the XRD patterns of Ni-NC, Fe-NC, and NC at around 26.3° and 44.4° correspond to the (002) and (101) planes of carbon, respectively. This effect can be attributed to the lower metal content and the presence of amorphous metals. Moreover, the position of the diffraction peaks of NiFe-NC does not change with respect to the change in pyrolysis temperature (Fig. S2†). The Raman spectrum of the electrocatalysts (Fig. 2b) shows two peaks at 1300 and 1650 cm^{-1}, which correspond to the D and G bands of carbon, respectively. The introduction of metals results in a slight increase in the intensity ratio of the D and G bands, implying an increase in the degree of defects and catalytic activity of the material.[33] Notably, the degree of defects in the catalyst is the highest when Ni and Fe bimetals are introduced simultaneously. Furthermore, the intensity ratio between the D and G bands reaches a maximum at 1000 °C with increasing temperature (Fig. S3†), indicating that NiFe-NC has more intrinsic defects.

The surface compositions and valence states were further investigated by X-ray photoelectron spectroscopy (XPS). The survey spectra (Fig. S4†) of NiFe-NC display all the C, N, O, Fe, and Ni peaks. The XPS spectrum of C 1s (Fig. 2c) can be divided into three peaks located at 284.8 eV, 285.7 eV, and 289 eV, corresponding to C–C, C–N, and O–C=O, respectively.[31] The high-resolution XPS spectra of N 1s in Fig. 2d reveal the nitrogen composition consisting of pyridinic N (398.5 eV), pyrrolic N (399.3 eV), graphitic N (401.2 eV), and oxidized N (405.1 eV).[1,34] Catalysts with a higher graphitic nitrogen content exhibit higher current density and higher CO selectivity,[35] whereas pyridinic nitrogen is regarded as the main catalytically active species for the ORR.[36] Moreover, this result again confirms the successful nitrogen doping in carbon.[37] The high-resolution XPS pattern of Fe 2p shown in Fig. 2e has peaks at 707.4 eV and 720.1 eV, corresponding to Fe^0, indicating the presence of metallic Fe. The peaks at 710.9 eV and 724.8 eV belong to Fe^{2+}. The Ni 2p XPS spectrum (Fig. 2f) also confirms the presence of nickel in the zero-valence state (852.8 and 870 eV), corresponding to metallic Ni in the NiFe alloy.[38]
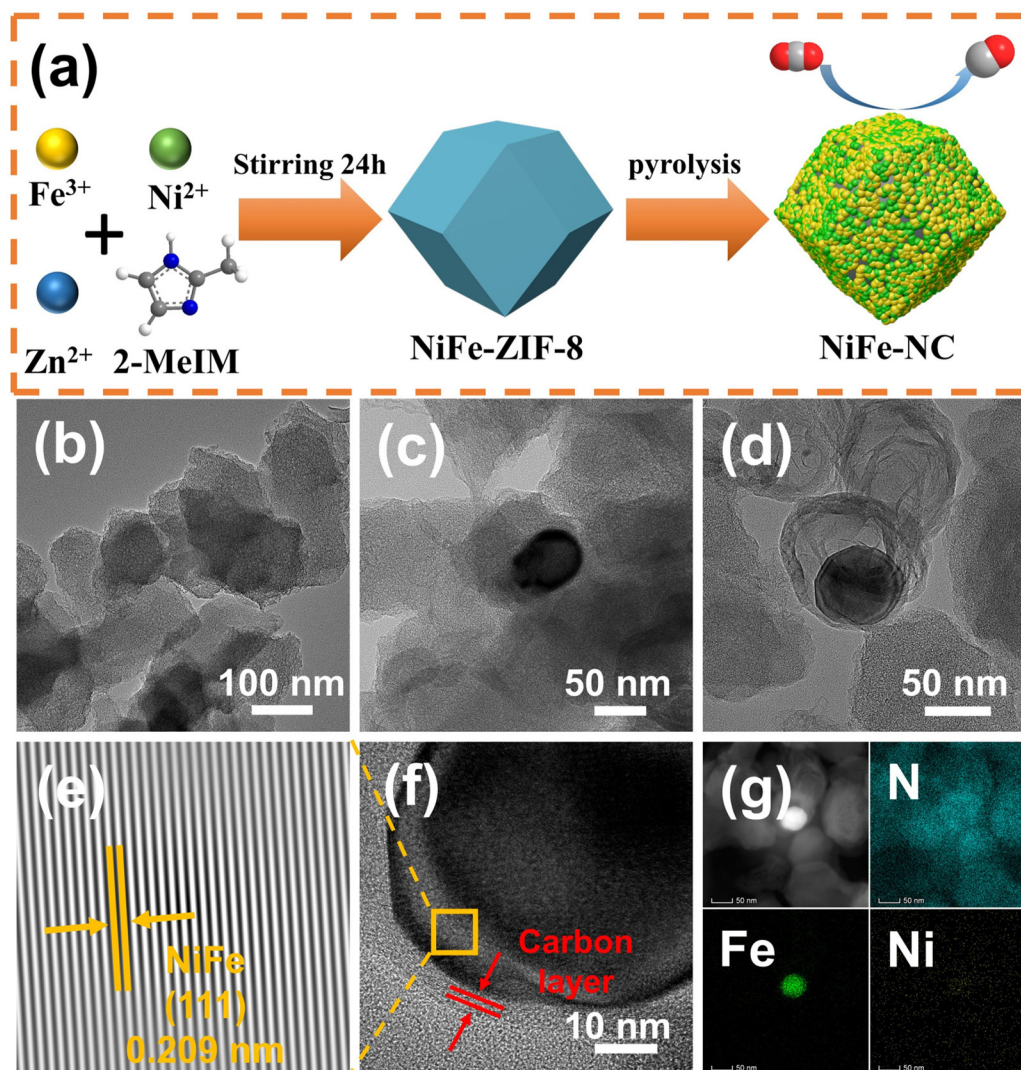
This journal is © the Partner Organisations 2023

Inorg. Chem. Front., 2023, **10**, 4484–4495 | **4485**

Fig. 1 (a) Schematic illustration of the synthesis of the electrode material; (b–d) TEM images of NiFe-NC; (e and f) HRTEM images and the magnified image of the selected region for the NiFe alloy nanoparticles; and (g) HAADF-STEM image and EDS elemental mapping images of NiFe-NC.

Additionally, the peaks centered at 855.7 and 873 eV are assigned to Ni^{2+}, which may be caused by surface oxidation.

2.2. Electrocatalytic performance for CO_2RR

The electrochemical CO_2 reduction performance of NiFe-NC was initially examined in an H-type electrolyzer, and to provide a basis for comparison, the CO_2RR performance of other samples was also evaluated. As revealed by the linear sweep voltammetry (LSV) curves (Fig. 3a and Fig. S5a†), NiFe-NC exhibits significantly enhanced current density, reflecting superior catalytic activity relative to the other control groups. The gaseous products from the CO_2RR were quantified using online gas chromatography (GC), revealing NiFe-NC's exceptionally high selectivity (>90%) for the CO product, with the highest faradaic efficiency for CO (FE_{CO}) of 93.42% at −0.58 V *vs.* RHE (Fig. 3b, Fig. S5b and c†). Impressively, NiFe-NC also maintains a high selectivity for CO (>90%) over a broad poten-

tial window (−0.38 to −0.68 V *vs.* RHE). The CO partial current density (j_{CO}) was further calculated for each catalyst, wherein the incorporation of the NiFe alloy resulted in a noteworthy increase in j_{CO}. The maximum j_{CO} for NiFe-NC was achieved at a pyrolysis temperature of 1000 °C (Fig. 3c and Fig. S5d†). At −0.78 V *vs.* RHE, NiFe-NC achieves an impressive CO partial current density of 15.06 mA cm^{-2}. Furthermore, the long-term stability of NiFe-NC (Fig. 3d) demonstrates no significant decrease in current density or FE_{CO} even after 12 h of continuous operation at −0.58 V *vs.* RHE, underscoring the excellent stability of this catalyst. Overall, these results establish the exceptional electrocatalytic performance of NiFe-NC and highlight its promising potential for CO_2 reduction applications.

To confirm the intrinsic catalytic activity of NiFe-NC, various electrochemical measurements, including the Tafel slope, electrochemical impedance spectrum (EIS) and electro-
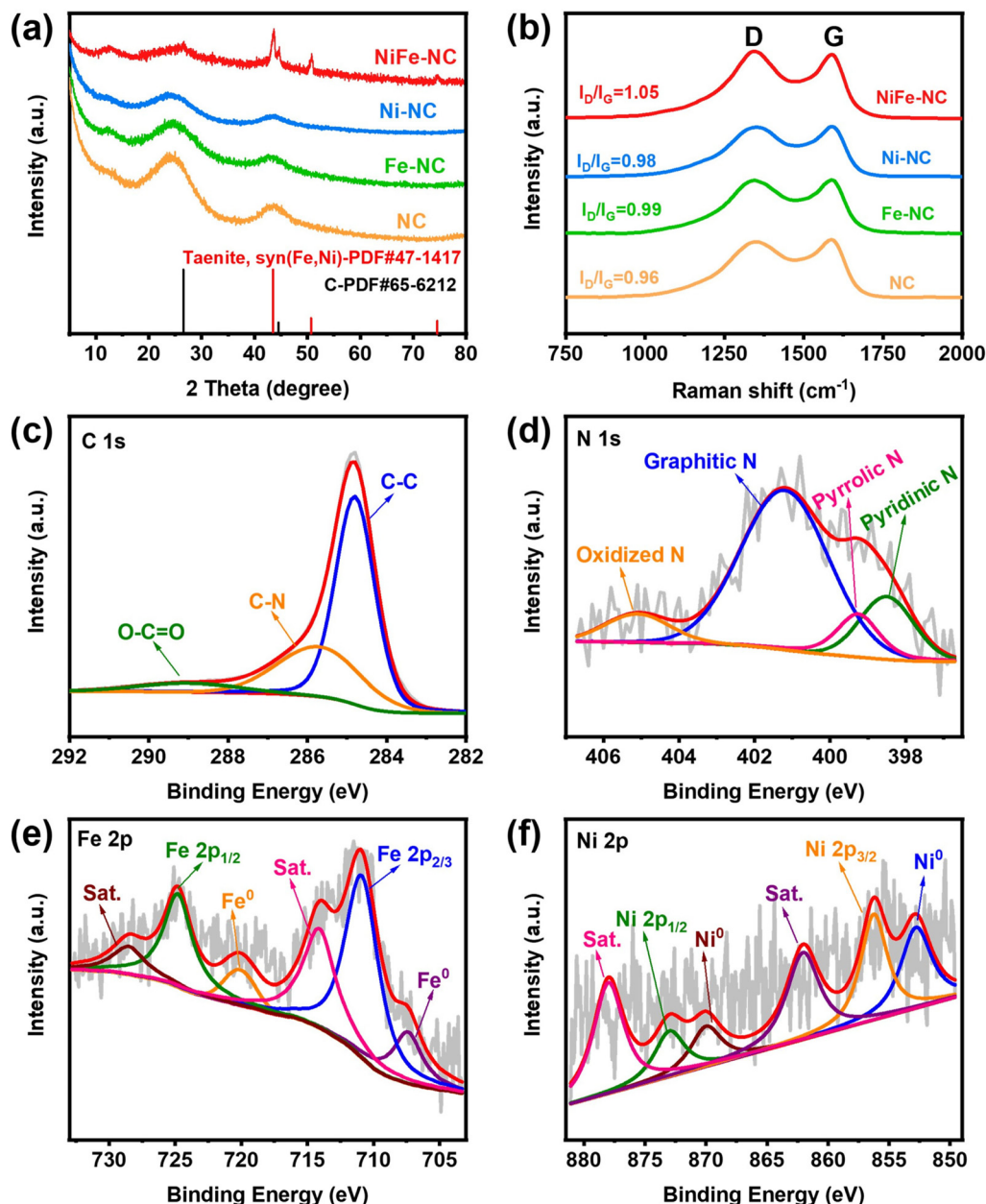
4486 | *Inorg. Chem. Front.*, 2023, **10**, 4484–4495

This journal is © the Partner Organisations 2023

Fig. 2 (a) XRD patterns and (b) Raman spectra of NiFe-NC, Fe-NC, Ni-NC, and NC; (c) C 1s, (d) N 1s, (e) Fe 2p, and (f) Ni 2p high-resolution XPS spectrum of NiFe-NC.

chemical surface area (ECSA), were measured. The Tafel slope of NiFe-NC was found to be 264 mV dec^{-1}, which is lower than those of the contrast samples (390 mV dec^{-1} for Ni-NC and 284 mV dec^{-1} for Fe-NC) (Fig. 3e). The lower Tafel slope of NiFe-N–C indicates a faster reaction kinetic process for CO$_2$RR.[39] Moreover, the EIS analysis (Fig. S6†) indicated that NiFe-NC exhibits the lowest charge transfer resistance compared to all the control samples, indicating its fast charge transfer ability. The double-layer capacitance (C_{dl}) is calculated as a reference for ECSA (Fig. 3f, Fig. S7 and 8†), and the results reveal that NiFe-NC possesses a higher C_{dl} value of 284.87 mF cm^{-2} compared to the other control samples, indicating the

presence of the highest number of active sites, which is consistent with its excellent CO$_2$RR activity.

Although H-cells are useful for pre-screening catalysts, their effectiveness is limited by the mass transport limitations of CO$_2$, which has low solubility in most aqueous solutions.[40] To further demonstrate the high activity and selectivity of the NiFe-NC catalyst in producing CO products by CO$_2$RR at industrial current densities, a flow cell electrolyzer was constructed. The configuration of the flow electrolytic cell is depicted in Fig. 4a, which employed 1 × 1 cm^2 carbon paper gas diffusion electrode (GDE) as a substrate, with 1.0 mg cm^{-2} of the catalyst deposited onto it. A proton exchange membrane (Nafion 117)

This journal is © the Partner Organisations 2023

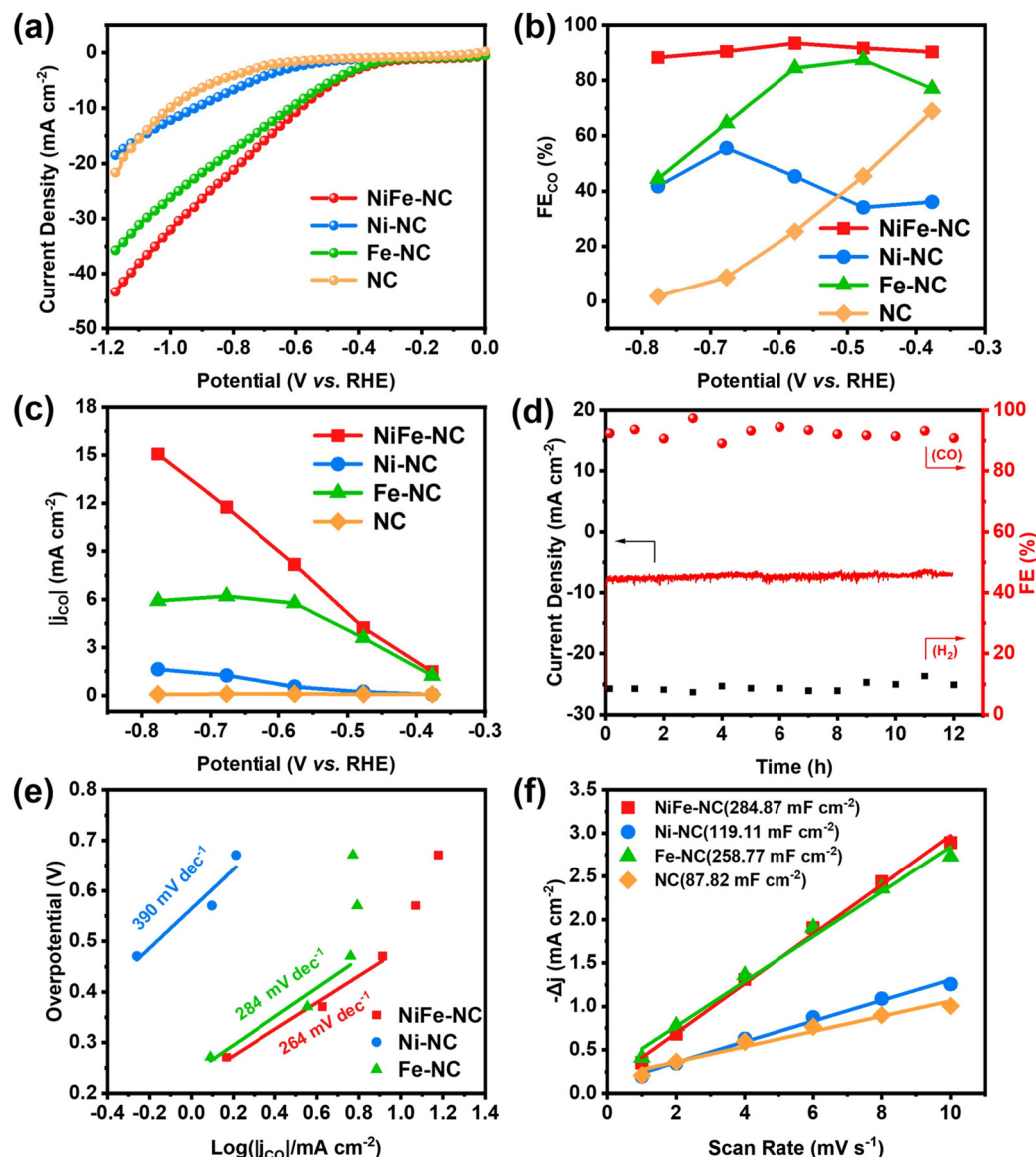*Inorg. Chem. Front.*, 2023, **10**, 4484–4495 | **4487**

Fig. 3 (a) LSV curves of the prepared catalysts measured in CO_2-saturated 0.5 M $KHCO_3$ electrolyte; (b) FE_{CO} and (c) CO partial current density of the prepared catalysts; (d) stability test for NiFe-NC at −0.58 V *vs.* RHE with 12 h of continuous electrolysis; (e) Tafel plots for the CO partial current density of different samples; and (f) the electrochemical double-layer capacitances of different samples.

was placed between the cathode (NiFe-NC GDE) and anode catalyst (Ni foam). The catholyte and anolyte were 3 M KCl and 1 M KOH, respectively, and were continuously circulated through the cathode and anode using a pump. CO_2 was continuously supplied to the cathode at a flow rate of 20 cm^3 min^{-1} throughout the test. The experiments were carried out in a constant voltage mode. Compared to KOH and $KHCO_3$ solutions, KCl solution has been reported to exhibit partial effectiveness in inhibiting carbonate deposition.[41] Moreover, a high concentration of K^+ has been found to increase the selectivity of CO_2 reduction and hinder the hydrogen evolution reaction.[42] As shown in Fig. 4b and Fig. S9a,† the utilization of the flow cell with 3 M KCl catholyte significantly improves the current density, with NiFe-NC demonstrating notably higher

performance. The selectivity of NiFe-NC for CO remains above 90% over a broad voltage range of −0.39 to −1.19 V *vs.* RHE, and the highest FE_{CO} is up to 98.88% at −0.59 V *vs.* RHE. Notably, at −1.19 V *vs.* RHE, the current density of NiFe-NC reaches 241.09 mA cm^{-2}, and the FE_{CO} is as high as 91.6% (Fig. 4c, Fig. S9b and c†). Remarkably, the recorded FE_{CO} and current density values achieved with NiFe-NC are notably higher than the catalysts from a previously reported reference in Table S2.† Furthermore, our results demonstrate that the flow cell can operate continuously for over 25 h at −0.59 V *vs.* RHE, while maintaining a stable current density of approximately 50 mA cm^{-2} and a high selectivity of over 90% for CO products (Fig. 4d), highlighting its favorable long-term stability.

4488 | *Inorg. Chem. Front.*, 2023, **10**, 4484–4495

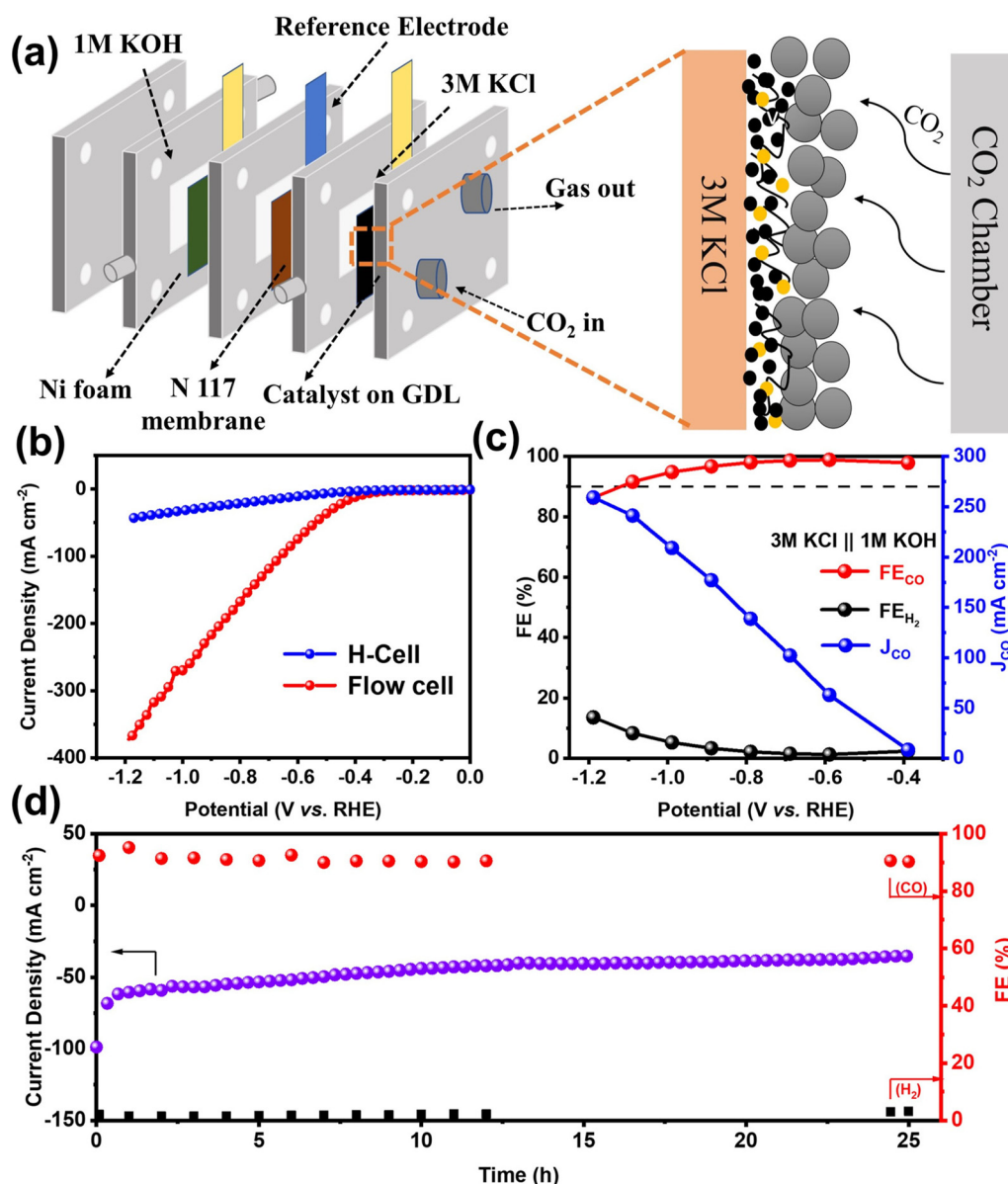This journal is © the Partner Organisations 2023

Fig. 4 (a) Schematic configuration of a flow cell reactor with a GDL loaded with catalyst; (b) LSV curves of NiFe-NC measured in the flow cell; (c) FE_{CO} and corresponding current densities of NiFe-NC in the flow cell; and (d) stability test for NiFe-NC at −0.59 V *vs.* RHE with 25 h of continuous electrolysis in the flow cell.

2.3. Electrocatalytic performance of ORR

Additionally, NiFe-NC also demonstrates an exceptional catalytic performance in the oxygen reduction reactions (ORR). To evaluate its ORR activity, cyclic voltammetry (CV) was employed in both argon- and O_2-saturated 0.1 M KOH solutions (Fig. S10†). When O_2 is introduced to the electrolyte, all materials, including commercial Pt/C, display a significant reduction peak, while the onset potential of NiFe-NC is close to that of Pt/C. Conversely, none of the catalysts exhibits ORR performance under Ar-saturated conditions. LSV curves were obtained in O_2-saturated 0.1 M KOH solution utilizing a rotating disk electrode (RDE) at 1600 rpm and a scan rate of 5 mV

s^{-1}. The LSV curves for NC, Ni-NC, Fe-NC, and commercial Pt/ C were also collected under the same conditions for comparison (Fig. 5a). The onset potential and half-wave potential of NiFe-NC demonstrate a remarkable similarity to those of Pt/C at 0.967 V *vs.* RHE, 0.867 V *vs.* RHE, and 0.956 V *vs.* RHE, 0.829 V *vs.* RHE, respectively, indicating that NiFe-NC exhibits ORR catalytic performance on par with that of Pt/C. Fig. 5b depicts the LSV test plots of NiFe-NC at various rotational speeds (400–2500 rpm), where the ultimate current density of NiFe-NC increases with increasing rotational speeds, suggesting a more uniform diffusion of O_2 on the electrode material. The Tafel curve in Fig. 5c shows the smallest slope of 67 mV dec^{-1} for NiFe-NC, indicating not only a higher catalytic current, but

This journal is © the Partner Organisations 2023

Inorg. Chem. Front., 2023, **10**, 4484–4495 | **4489**

Fig. 5 (a) ORR polarization curves of different catalysts in 0.1 M KOH; (b) ORR polarization curves of NiFe-NC at different speeds (rpm); (c) Tafel slope curve for the prepared catalysts; (d) open-circuit plots of ZABs; (e) discharge polarization curves and the corresponding power densities; and (f) rate discharge curves at various current densities.

also superior ORR activity. The K–L equation was used to compute the corresponding kinetic parameters of NiFe-NC (Fig. S11†), and the number of transferred electrons was determined to be close to a theoretical value of 4.0 for the ORR, signifying that the catalyst is efficient in the reduction of oxygen through a four-electron transfer pathway.

With NiFe-NC demonstrating outstanding catalytic activity for the ORR, we proceeded to construct a zinc–air battery, which comprised a zinc plate anode and an air cathode. The electrolyte used was 6 M KOH + 0.2 M $Zn(CH_3COO)_2$ solution. As depicted in Fig. 5d, the ZAB with NiFe-NC exhibits an open-circuit voltage of 1.416 V, which remains constant for 12 h. When two batteries were connected in series, a small bulb could be illuminated (Fig. S12†). Notably, the maximum power density of the ZAB coated with the NiFe-NC catalyst is

185.92 mW cm^{-2}, surpassing that of the ZAB coated with the Pt/C catalyst (Fig. 5e). This observation suggests that the prepared catalysts have higher catalytic activity and faster mass transfer process in ZAB.[43] We also evaluated the multiplicative discharge performance of ZAB at various current densities (2–20 mA cm^{-2}). As shown in Fig. 5f, the discharge potential plateau decreases with increasing current density.

2.4. Performance of a ZAB-powered CO_2 flow electrolysis system

Inspired by the exceptional performance of NiFe-NC catalysts in ZABs and CO_2RR, we assembled a self-driven CO_2 flow electrolysis system powered by homemade ZABs. The schematic diagram of the self-driven CO_2 flow electrolysis system powered by ZABs is illustrated in Fig. 6a, and a photograph of
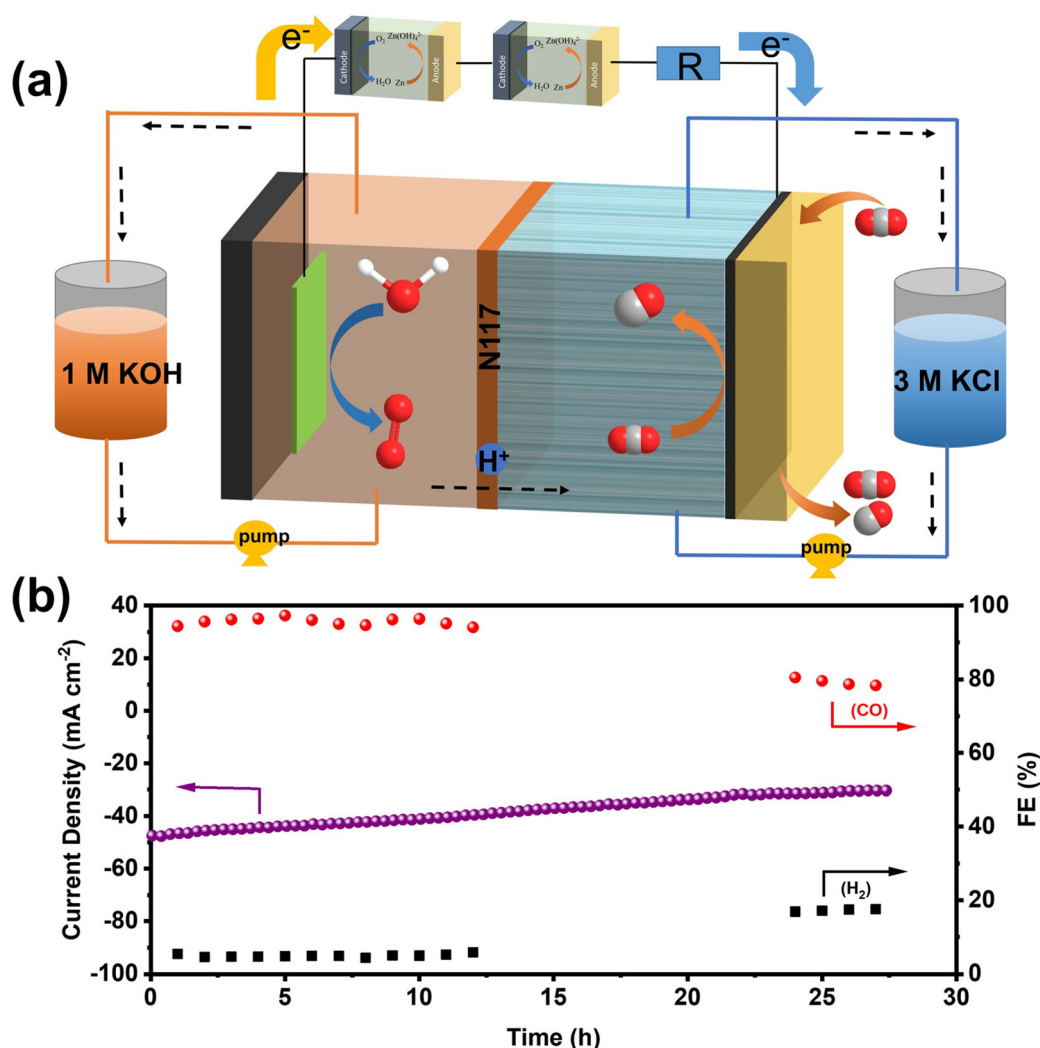
Fig. 6 (a) Schematic diagram of a self-driven CO_2 flow electrolysis system powered by two-series-connected homemade ZABs and (b) the current density and FE results in the self-driven CO_2 flow electrolysis systems.

the system is shown in Fig. S13.† Both ZAB and the CO_2RR flow electrolytic cell were assembled with NiFe-NC as cathodes. Two ZABs were connected in series with the flow electrolytic cell (used as the CO_2RR device) and a 10 Ω resistor (used to calculate the current in the circuit). As indicated in Fig. S14 and S15,† the voltage across the resistor and the CO_2 flow electrolytic system is 0.471 V and 1.83 V, respectively. The products from the self-driven CO_2 flow electrolysis system were detected by GC, and a voltage collector was utilized to collect the voltage across the resistor, thereby obtaining the current of the CO_2 flow electrolysis system. As shown in Fig. 6b, at the start of operation, the self-driven CO_2 flow electrolysis system exhibits a current density of ~47 mA cm^{-2} with an FE_{CO} of ~95%. After 27 h of continuous operation, the current density is maintained at ~30 mA cm^{-2}, and the FE_{CO} is reduced to 68.35%. The decrease in device performance may be due to the continuous consumption of the anode zinc plate to form zinc oxide, which covers the surface

of the zinc plate and inhibits self-driven reduction.[44,45] Nevertheless, these results demonstrate the feasibility of a self-driven CO_2 flow electrolysis system powered by ZABs, offering a new strategy for industrial-level CO_2 reduction without additional energy input.

2.5. Density functional theory calculations

We were able to identify the underlying cause for the excellent CO_2RR performance of the NiFe-NC catalyst by using a density functional theory (DFT)-based approach. We ran calculations on all potentially active sites on the NiFe-NC catalyst, including pyrrole edge (pyrroleNH), N-doped graphene (GN), dual N-doped graphene (GNN), armchair edge sites of pyridinic N with and without hydrogenation (ApyN and ApyNH) and zigzag edge sites with and without hydrogenation (ZpyN and ZpyNH), which are all depicted in Fig. S16.† In prior research, it was claimed that these locations were exposed to CO_2RR and ORR.[43,46] Furthermore, we constructed the structure of gra-
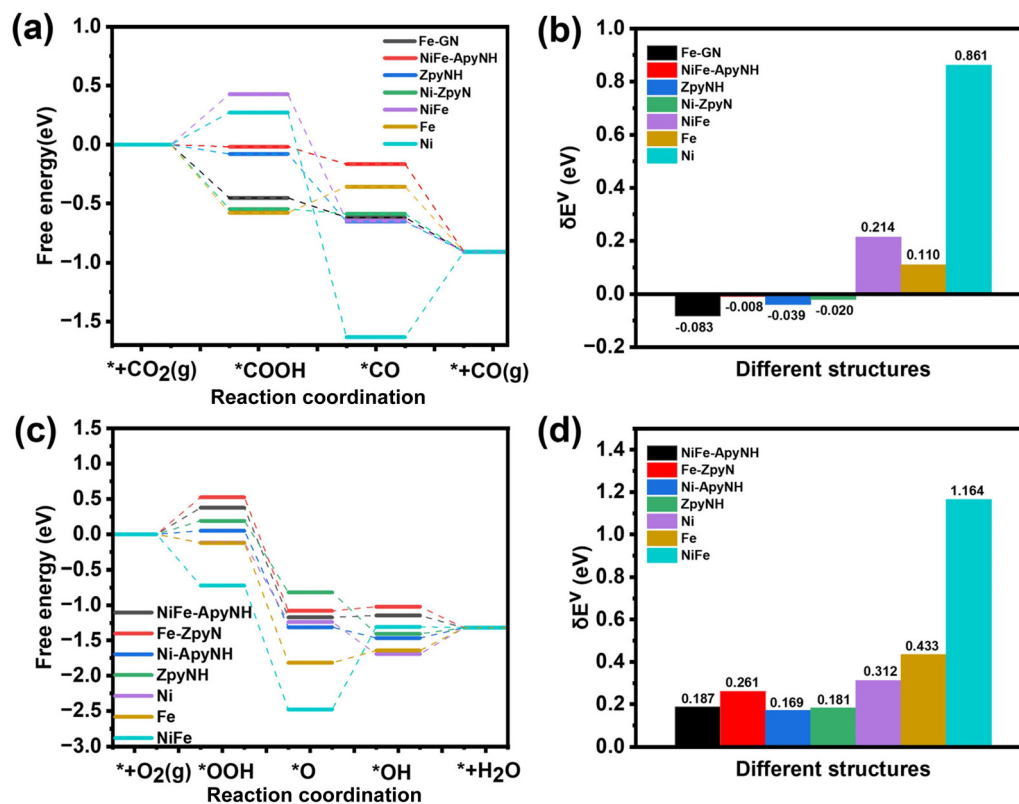
This journal is © the Partner Organisations 2023

Inorg. Chem. Front., 2023, **10**, 4484–4495 | **4491**

Fig. 7 The free energy diagrams (FEDs) of CO_2RR (a) and ORR (c) on optimal active site for each type; (b) the δE^v values of CO_2RR (b) and ORR (d) on the optimal active site for each type.

phene-covered metals using the experimental TEM image (Fig. 1f) as a basis. This includes graphene-covered Ni clusters (Ni-ApyN, Ni-ApyNH, Ni-ZpyN, Ni-ZpyNH, Ni-pyrroleNH, Ni-GN, and Ni-GNN, as shown in Fig. S17†), graphene-covered Fe clusters (Fe-ApyN, Fe-ApyNH, Fe-ZpyN, Fe-ZpyNH, Fe-pyrroleNH, Fe-GN, and Fe-GNN, as demonstrated in Fig. S18†), and graphene-covered NiFe alloy clusters (NiFe-ApyN, NiFe-ApyNH, NiFe-ZpyN, NiFe-ZpyNH, NiFe-pyrrole NH, NiFe-GN, and NiFe-GNN, as displayed in Fig. S19†). To compare the structural properties of metals covered by graphene, we generated the structures of Ni, Fe, and NiFe alloys without the graphene coverage, which are shown in Fig. S20.† The energy profiles of the reactions were calculated using the computational hydrogen electrode (CHE) method,[47] with the virtual energetic span (δE^v) serving as the activity-determining term.[48] Detailed information is provided in Section 2 of the ESI.† We performed CO_2RR and ORR calculations on all possible active sites on graphene-covered metals, as shown in Fig. S21 and S22.† Our analysis reveals that the optimal active sites for CO_2RR are Z-pyNH, Ni-pyN, Fe-GN, and NiFe-ApyNH (Fig. 7a), whereas the optimal active sites for ORR are NiFe-ApyNH, Fe-ZpyN, Ni-ApyNH, and ZpyNH (Fig. 7c). Based on the virtual energetic span (δE^v), as shown in Fig. 7b and d, we discover that the Ni-ApyNH (0.169 eV) structure is the best active site for ORR, and the Fe-GN (−0.083 eV) structure is the best active site for CO_2RR. This is consistent with the experimental results and

shows that Fe is more beneficial for CO_2RR in NiFe-NC catalysts whereas Ni is more favorable for the ORR.

3. Conclusions

To summarize, our study has demonstrated the outstanding electrocatalytic performance of the NiFe-NC catalyst synthesized through a simple pyrolysis method. Our autonomously built flow cell reactor achieves an impressive industrial current density of 241.09 mA cm^{-2} and maintains a high FE of 91.6% without any decay for 25 h at 50 mA cm^{-2}. Impressively, this performance also outstrips that of the majority of reported catalysts for CO_2RR, underlining the exceptional electrocatalytic properties of the NiFe-NC catalyst. Furthermore, we investigate the potential of NiFe-NC in zinc–air batteries, which shows a maximum power density of 185.92 mW cm^{-2}. Our work provides a compelling approach to explore cost-effective bifunctional electrocatalysts for both CO_2RR and ORR, with a promising prospect of simplifying electrocatalyst systems in electrochemical applications. In particular, we design a self-driven CO_2 flow electrolysis system that holds great potential for industrial applications. This system is powered by two NiFe-NC-based ZABs connected in series and represents an innovative approach for energy conversion. DFT calculations show that the Fe site in the bimetallic material

contributes more to CO_2RR, while the Ni site in the bimetallic material plays a more important role in ORR. The synergistic effect of bimetals promotes the electrocatalytic reaction. We believe that our work provides an in-depth understanding of the catalytic mechanism of bimetallic active sites, and the bifunctional electrocatalyst we developed, NiFe-NC, will be promising for applications in flow electrolytic cells and zinc–air batteries.

Author contributions

Songjiang Wu: conceptualization, methodology, data curation, writing – original draft, investigation, formal analysis, and visualization. Haiyan Chen: methodology, formal analysis, investigation, and writing – review & editing. Chunguang Jia: software. Li Liao: methodology. Kai Chen: visualization. Suqin Ci: supervision, writing – review & editing, and funding acquisition. Qiuhua Xu: supervision. Zhenhai Wen: methodology, supervision, funding acquisition, and resources.

Conflicts of interest

There are no conflicts to declare.

Acknowledgements

References

1 Y. Zhou, M. Xie, Y. Song, D. Yan, Z. Wang, S. Zhang and C. Deng, Edge-enriched Ni-N_4 atomic sites embedded enoki-mushroom-like carbon nanotubes assembling hollow fibers for CO_2 conversion and flexible Zn–air battery, *Energy Storage Mater.*, 2022, **47**, 235–248.

2 M. Feng, X. Wu, H. Cheng, Z. Fan, X. Li, F. Cui, S. Fan, Y. Dai, G. Lei and G. He, Well-defined Fe–Cu diatomic sites for efficient catalysis of CO_2 electroreduction, *J. Mater. Chem. A*, 2021, **9**, 23817–23827.

3 X. Yu, T. Zhou, J. Ge and C. Wu, Recent advances on the modulation of electrocatalysts based on transition metal nitrides for the rechargeable Zn–air battery, *ACS Mater. Lett.*, 2020, **2**, 1423–1434.

4 H. Mistry, A. S. Varela, S. Kühl, P. Strasser and B. R. Cuenya, Nanostructured electrocatalysts with tunable activity and selectivity, *Nat. Rev. Mater.*, 2016, **1**, 1–14.

5 C. Chen, J. F. K. Kotyk and S. W. Sheehan, Progress toward commercial application of electrochemical carbon dioxide reduction, *Chem*, 2018, **4**, 2571–2586.

6 T. Tang, Z. Wang and J. Guan, Optimizing the electrocatalytic selectivity of carbon dioxide reduction reaction by regulating the electronic structure of single-atom M-N-C materials, *Adv. Funct. Mater.*, 2022, **32**, 2111504.

7 X. Shu, Q. Chen, M. Yang, M. Liu, J. Ma and J. Zhang, Tuning Co-catalytic sites in hierarchical porous N-doped carbon for high-performance rechargeable and flexible Zn–air battery, *Adv. Energy Mater.*, 2022, **13**, 2202871.

8 S. J. Cobb, V. M. Badiani, A. M. Dharani, A. Wagner, S. Zacarias, A. R. Oliveira, I. A. C. Pereira and E. Reisner, Fast CO_2 hydration kinetics impair heterogeneous but improve enzymatic CO_2 reduction catalysis, *Nat. Chem.*, 2022, **14**, 417–424.

9 H. Zhang, T. Wei, Y. Qiu, S. Zhang, Q. Liu, G. Hu, J. Luo and X. Liu, Recent progress in metal phosphorous chalcogenides: Potential high-performance electrocatalysts, *Small*, 2023, **19**, 2207249.

10 Y. S. Ham, Y. S. Park, A. Jo, J. H. Jang, S.-K. Kim and J. J. Kim, Proton-exchange membrane CO_2 electrolyzer for CO production using Ag catalyst directly electrodeposited onto gas diffusion layer, *J. Power Sources*, 2019, **437**, 226898.

11 Z.-H. Gao, K. Wei, T. Wu, J. Dong, D.-e. Jiang, S. Sun and L.-S. Wang, A heteroleptic gold hydride nanocluster for efficient and selective electrocatalytic reduction of CO_2 to CO, *J. Am. Chem. Soc.*, 2022, **144**, 5258–5262.

12 T. Zhang, X. Han, H. Liu, M. Biset-Peiró, J. Li, X. Zhang, P. Tang, B. Yang, L. Zheng, J. R. Morante and J. Arbiol, Site-specific axial oxygen coordinated fen_4 active sites for highly selective electroreduction of carbon dioxide, *Adv. Funct. Mater.*, 2022, **32**, 2111446.

13 C. Wang, Y. Liu, H. Ren, Q. Guan, S. Chou and W. Li, Diminishing the uncoordinated N species in Co-N-C catalysts toward highly efficient electrochemical CO_2 reduction, *ACS Catal.*, 2022, **12**, 2513–2521.

14 Y. Guo, S. Yao, Y. Xue, X. Hu, H. Cui and Z. Zhou, Nickel single-atom catalysts intrinsically promoted by fast pyrolysis for selective electroreduction of CO_2 into CO, *Appl. Catal., B*, 2022, **304**, 120997.

15 T. Wang, S. Gao, T. Wei, Y. Qin, S. Zhang, J. Ding, Q. Liu, J. Luo and X. Liu, Co nanoparticles confined in mesoporous Mo/N Co-doped polyhedral carbon frameworks towards high-efficiency oxygen reduction, *Chem. – Eur. J.*, 2023, **29**, e202204034.

16 C. Kim, F. Dionigi, V. Beermann, X. Wang, T. Möller and P. Strasser, Alloy nanocatalysts for the electrochemical oxygen reduction (ORR) and the direct electrochemical carbon dioxide reduction reaction (CO_2RR), *Adv. Mater.*, 2018, **31**, 1805617.

17 Q. Zhang, K. Lian, Q. Liu, G. Qi, S. Zhang, J. Luo and X. Liu, High entropy alloy nanoparticles as efficient catalysts for alkaline overall seawater splitting and Zn–air batteries, *J. Colloid Interface Sci.*, 2023, **646**, 844–854.

18 X. She, Y. Wang, H. Xu, S. C. E. Tsang and S. P. Lau, Challenges and opportunities in electrocatalytic CO_2

This journal is © the Partner Organisations 2023

Inorg. Chem. Front., 2023, **10**, 4484–4495 | **4493**

reduction to chemicals and fuels, *Angew. Chem., Int. Ed.*, 2022, **61**, e202211396.

19 D. Wu, F. Jiao and Q. Lu, Progress and understanding of CO_2/CO electroreduction in flow electrolyzers, *ACS Catal.*, 2022, **12**, 12993–13020.

20 Z.-Z. Niu, L.-P. Chi, R. Liu, Z. Chen and M.-R. Gao, Rigorous assessment of CO_2 electroreduction products in a flow cell, *Energy Environ. Sci.*, 2021, **14**, 4169–4176.

21 S. Ren, D. Joulié, D. Salvatore, K. Torbensen, M. Wang, M. Robert and C. P. Berlinguette, Molecular electrocatalysts can mediate fast, selective CO_2 reduction in a flow cell, *Science*, 2019, **365**, 367–369.

22 T. Wei, S. Zhang, Q. Liu, Y. Qiu, J. Luo and X. Liu, Oxygen vacancy-rich amorphous copper oxide enables highly selective electroreduction of carbon dioxide to ethylene, *Acta Phys.-Chim. Sin.*, 2022, **39**, 202207026.

23 X. Wang, S. Liu, H. Zhang, S. Zhang, G. Meng, Q. Liu, Z. Sun, J. Luo and X. Liu, Polycrystalline SnS_x nanofilm enables CO_2 electroreduction to formate with high current density, *Chem. Commun.*, 2022, **58**, 7654–7657.

24 F. Pan, B. Li, E. Sarnello, S. Hwang, Y. Gang, X. Feng, X. Xiang, N. M. Adli, T. Li, D. Su, G. Wu, G. Wang and Y. Li, Boosting CO_2 reduction on Fe–N–C with sulfur incorporation: Synergistic electronic and structural engineering, *Nano Energy*, 2020, **68**, 104384.

25 W. Ju, A. Bagger, G.-P. Hao, A. S. Varela, I. Sinev, V. Bon, B. R. Cuenya, S. Kaskel, J. Rossmeisl and P. Strasser, Understanding activity and selectivity of metal-nitrogen-doped carbon catalysts for electrochemical reduction of CO_2, *Nat. Commun.*, 2017, **8**, 944.

26 Q. Lu, C. Chen, Q. Di, W. Liu, X. Sun, Y. Tuo, Y. Zhou, Y. Pan, X. Feng, L. Li, D. Chen and J. Zhang, Dual role of pyridinic-N doping in carbon-coated Ni nanoparticles for highly efficient electrochemical CO_2 reduction to CO over a wide potential range, *ACS Catal.*, 2022, **12**, 1364–1374.

27 F. Wang, Z. Miao, J. Mu, Y. Zhao, M. Liang, J. Meng, X. Wu, P. Zhou, J. Zhao, S. Zhuo and J. Zhou, A Ni nanoparticles encapsulated in N-doped carbon catalyst for efficient electroreduction CO_2: Identification of active sites for adsorption and activation of CO_2 molecules, *Chem. Eng. J.*, 2022, **428**, 131323.

28 Z. Zeng, L. Y. Gan, H. Yang, X. Su, J. Gao, W. Liu, H. Matsumoto, J. Gong, J. Zhang, W. Cai, Z. Zhang, Y. Yan, B. Liu and P. Chen, Orbital coupling of hetero-diatomic nickel-iron site for bifunctional electrocatalysis of CO_2 reduction and oxygen evolution, *Nat. Commun.*, 2021, **12**, 4088.

29 Y. Li, W. Shan, M. J. Zachman, M. Wang, S. Hwang, H. Tabassum, J. Yang, X. Yang, S. Karakalos, Z. Feng, G. Wang and G. Wu, Atomically dispersed dual-metal site catalysts for enhanced CO_2 reduction: Mechanistic insight into active site structures, *Angew. Chem., Int. Ed.*, 2022, **61**, e202205632.

30 R. Yun, F. Zhan, X. Wang, B. Zhang, T. Sheng, Z. Xin, J. Mao, S. Liu and B. Zheng, Design of binary Cu–Fe sites coordinated with nitrogen dispersed in the porous carbon for synergistic CO_2 electroreduction, *Small*, 2020, **17**, 2006951.

31 L. Yan, Y. Xu, P. Chen, S. Zhang, H. Jiang, L. Yang, Y. Wang, L. Zhang, J. Shen, X. Zhao and L. Wang, A freestanding 3D heterostructure film stitched by MOF-derived carbon nanotube microsphere superstructure and reduced graphene oxide sheets: A superior multifunctional electrode for overall water splitting and Zn–air batteries, *Adv. Mater.*, 2020, **32**, 2003313.

32 H. Lei, Z. Wang, F. Yang, X. Huang, J. Liu, Y. Liang, J. Xie, M. S. Javed, X. Lu, S. Tan and W. Mai, NiFe nanoparticles embedded N-doped carbon nanotubes as high-efficient electrocatalysts for wearable solid-state Zn–air batteries, *Nano Energy*, 2020, **68**, 104293.

33 P. Pachfule, D. Shinde, M. Majumder and Q. Xu, Fabrication of carbon nanorods and graphene nanoribbons from a metal–organic framework, *Nat. Chem.*, 2016, **8**, 718–724.

34 X. Han, T. Zhang, X. Wang, Z. Zhang, Y. Li, Y. Qin, B. Wang, A. Han and J. Liu, Hollow mesoporous atomically dispersed metal-nitrogen-carbon catalysts with enhanced diffusion for catalysis involving larger molecules, *Nat. Commun.*, 2022, **13**, 2900.

35 Z. Zhang, L. Yu, Y. Tu, R. Chen, L. Wu, J. Zhu and D. Deng, Unveiling the active site of metal-free nitrogen-doped carbon for electrocatalytic carbon dioxide reduction, *Cell Rep. Phys. Sci.*, 2020, **1**, 100145.

36 L. Lai, J. R. Potts, D. Zhan, L. Wang, C. K. Poh, C. Tang, H. Gong, Z. Shen, J. Lin and R. S. Ruoff, Exploration of the active center structure of nitrogen-doped graphene-based catalysts for oxygen reduction reaction, *Energy Environ. Sci.*, 2012, **5**, 7936–7942.

37 K. Chen, Z. Wen, P. Cai, G. Wang, S. Ci and K. Li, One-pot scalable route to tri-functional electrocatalysts $FeCoP_X$ nanoparticles for integrated electrochemical devices, *Appl. Catal., B*, 2021, **295**, 120275.

38 L. Yang, X. Zeng, D. Wang and D. Cao, Biomass-derived FeNi alloy and nitrogen-codoped porous carbons as highly efficient oxygen reduction and evolution bifunctional electrocatalysts for rechargeable Zn–air battery, *Energy Storage Mater.*, 2018, **12**, 277–283.

39 F. Wang, G. Wang, P. Deng, Y. Chen, J. Li, D. Wu, Z. Wang, C. Wang, Y. Hua and X. Tian, Ultrathin nitrogen–doped carbon encapsulated ni nanoparticles for highly efficient electrochemical CO_2 reduction and aqueous Zn–CO_2 batteries, *Small*, 2023, **19**, 2301128.

40 D. Xu, K. Li, B. Jia, W. Sun, W. Zhang, X. Liu and T. Ma, Electrocatalytic CO_2 reduction towards industrial applications, *Carbon Energy*, 2022, **5**, e230.

41 Q. Fan, P. Gao, S. Ren, Y. Qu, C. Kong, J. Yang and Y. Wu, Total conversion of centimeter-scale nickel foam into single atom electrocatalysts with highly selective CO_2 electrocatalytic reduction in neutral electrolyte, *Nano Res.*, 2022, **16**, 2003–2010.

42 J. E. Huang, F. Li, A. Ozden, A. S. Rasouli and A. S. Rasouli, CO_2 electrolysis to multicarbon products in strong acid, *Science*, 2021, **372**, 1074–1078.

43 J. Li, Z. Wen, Q. Xu, K. Chen, T. Zhang, J. Wu and S. Ci, N-doped carbon networks as bifunctional electrocatalyst toward integrated electrochemical devices for Zn–air batteries driving microbial CO_2 electrolysis cell, *J. CO_2 Util.*, 2022, **62**, 102068.

44 S. Gao, T. Wang, M. Jin, S. Zhang, Q. Liu, G. Hu, H. Yang, J. Luo and X. Liu, Bifunctional Nb–N–C atomic catalyst for aqueous Zn–air battery driving CO_2 electrolysis, *Sci. China Mater.*, 2022, **66**, 1013–1023.

45 S. Gao, M. Jin, J. Sun, X. Liu, S. Zhang, H. Li, J. Luo and X. Sun, Coralloid Au enables high-performance Zn–CO_2 battery and self-driven CO production, *J. Mater. Chem. A*, 2021, **9**, 21024–21031.

46 Y. Wang, J. Chen, G. Wang, Y. Li and Z. Wen, Perfluorinated covalent triazine framework derived hybrids for the highly selective electroconversion of carbon dioxide into methane, *Angew. Chem., Int. Ed.*, 2018, **57**, 13120–13124.

47 J. K. Nørskov, J. Rossmeisl, A. Logadottir, L. Lindqvist, J. R. Kitchin, T. Bligaard and H. Jónsson, Origin of the overpotential for oxygen reduction at a fuel-cell cathode, *J. Phys. Chem. B*, 2004, **108**, 17886–17892.

48 J. Chen, Y. Chen, P. Li, Z. Wen and S. Chen, Energetic span as a rate-determining term for electrocatalytic volcanos, *ACS Catal.*, 2018, **8**, 10590–10598.